Role of elastic and shear stabilities in the martensitic transformation path of NiTi

N. Hatcher,[1] O. Yu. Kontsevoi,[1] and A. J. Freeman[1,2]
[1]*Department of Physics and Astronomy, Northwestern University, Evanston, Illinois 60208, USA*
[2]*Department of Materials Science and Engineering, Northwestern University, Evanston, Illinois 60208, USA*
(Received 20 July 2009; revised manuscript received 28 September 2009; published 20 October 2009)

Due to the importance of NiTi as a shape-memory material and the uncertainty regarding its atomisitic martensitic transformation path, a thorough investigation to understand the structural stability governing this displacive phase transformation is warranted. We investigate elastic and shear stabilities of NiTi using first-principles calculations with the highly precise full-potential linearized augmented plane-wave method. Ambiguities of the B2, R, B19, B19′, and proposed B33 structures are resolved, and we establish that the *P*3 symmetry is preferred for the R phase of equiatomic NiTi, and the phase stability of each structure is established by examining calculated formation energies, which show agreement with direct reaction calorimetry experiments. Additionally, all single-crystal elastic constants, Young's, bulk and shear moduli, Poisson's ratio, and the Zener anisotropy of the B2, R, B19, B19′, and B33 phases are calculated and presented yielding agreement with experiment that exceeds that of previous calculations. To investigate the susceptibility to shearing, generalized stacking-fault energetics are calculated for the {001}, {011}, and {111} slip planes of the B2 phase. Burgers vectors and shear resistance are established while examining atomic shuffling throughout the imposed shear; the {001} and {111} stacking faults possess high-energy barriers. By investigating various deformation mechanisms related to these stacking faults, we find an instability to ⟨100⟩{011} slip in the B2 phase. Using this and reviewing previously proposed atomistic transformation paths, the mechanisms governing the direct martensitic transformation of NiTi between the austenite and the martensite are identified. Barrierless transformation paths from the B2 phase to the B19′ phase and from the B2 phase to the B33 phase are proposed.

DOI: 10.1103/PhysRevB.80.144203 PACS number(s): 64.70.kd, 64.60.My, 68.35.Gy

I. INTRODUCTION

Equiatomic NiTi has generated significant interest for its exhibition of a reversible martensitic transformation near room temperature and is being utilized in applications which include medical devices such as surgical tools, orthodontic appliances, coronary probes, and stints, as well as materials for aerospace, industrial, and commercial use. Despite ample research on this material beginning in 1938 (Ref. 1) and a recent expansion of the literature devoted to NiTi,[2–6] much about this material is still not fully understood. Specifically, structures of the martensite and intermediate R phase have not been unambiguously established;[2,3] energy barriers between the phases are still unknown; recent independent elastic-constant calculations[4] have not been confirmed and calculated macroscopic moduli vary from experimental measurements; and, finally, there are several competing theories regarding the transformation path from the austenite to the martensite.[5–8] This paper will address these questions.

The complexity of this material is apparent in the multitude of its phases. In total, there are four different phases that were observed throughout the martensitic transformation of NiTi: (i) a B2 body-centered-cubic structure is its high-temperature austenitic phase. This phase was identified early in the study of NiTi (Refs. 8 and 9) and is now well established as the high-temperature austenite structure.[10] Intermediate phases of the martensitic transformation are also of particular interest as they occur at or near room temperature and give insight into NiTi's transition path. (ii) The R structure is an intermediate phase observed during the martensitic transformation for both equiatomic NiTi and NiTi alloyed with additions such as iron. The space group of this structure remains ambiguous despite electron and powder x-ray diffraction[11] and dynamic electron-diffraction[12] measurements, and theoretical pseudopotential calculations[3] since each of them suggests different space-group representations of the structure, namely, $P3$, $P\bar{3}$, and $P31m$, respectively. (iii) Another intermediate phase, the B19 structure, is observed[13,14] when NiTi is alloyed with at least 7.5% copper or certain percentages of other elements, such as Pd and Pt.[15,16] Varying the percentage of copper additions, Nam *et al.*[13] also discovered that B19 becomes the martensitic phase when NiTi is alloyed with at least 20% copper. The full characterization of these intermediate phases is incomplete and questions remain concerning their connection to the austenitic and martensitic phases. (iv) It has been generally agreed by experimentalists and theorists[8,9,17–19] that the monoclinic B19′ structure is the low-temperature martensite of NiTi. In recent experiments, Prokoshkin *et al.*[17] showed that the B19′ structure was stable from −20 °C to 80 °C. By studying different compositions of NiTi over this temperature range with different methods of aging and quenching, they determined the lattice constants and monoclinic angle in equiatomic and near-equiatomic NiTi. In all cases they found a $P2_1/m$ structure with a monoclinic angle between 96° and 98°.

However, recent first-principles calculations have raised doubts about the martensitic phase of NiTi. Huang *et al.*[2] proposed that a base-centered orthorhombic (BCO) structure of space group *Cmcm* is the martensitic phase and claimed that the experimentally reported B19′ structure is stabilized by internal stresses. Recently, Morris *et al.*[6] proposed a trans-

formation that involves bilayer ⟨100⟩{011} shear along with a "shuffling" of the atomic positions for B2 ordered intermetallics. They suggest that this shuffle leads to the *Cmcm* space-group structure postulated by Huang *et al.*; this structure was identified as B33 and they reported that the transformation path to the B33 phase has no energy barrier. Subsequently, Wagner and Windl[4] confirmed the existence and stability of this phase near $T=0$ in extensive calculations of its elastic properties and calculated the stresses needed to stabilize the B19′ structure. The present authors confirmed many of these results[5] and we report additional findings here.

In this paper, we investigate the B2, R, B19, B19′, and B33 structures of NiTi in order to identify the governing processes of the transformation using fully first-principles calculations. First, computational details are explained in Sec. II including an explanation of the full structural optimization employed with each phase. Phase energetics and structural stabilities, including calculated total-energy differences and formation energies, are reported in Sec. III A. Also included there are our results on several proposed space groups of the R phase[3,11,20,21] and on calculations of the B33 structure. For each phase of the martensitic transformation, all independent elastic moduli have been calculated in Sec. III B. To investigate shear instabilities, generalized stacking-fault calculations were performed and these results are shown in Sec. III C for the {001}, {011}, and {111} slip planes of the B2 structure.

In Sec. III D, we report details of the transformation mechanism between the austenitic B2 and martensitic B19′ phases, which we previously described.[5] This transformation may be accomplished by an atomic bilayer shear distortion along the {011} slip plane while simultaneously allowing full relaxation of the lattice constants and atomic positions. Comparing total energies of the optimized structures along the path, we find a barrierless transformation path from B2 to an intermediate point that is marked by a relative displacement along the slip plane of one half a lattice constant, 109°-B19′. Further calculations using this structure show an instability to monoclinic angle relaxation. Thus, a subsequent monoclinic angle relaxation causes a barrierless transformation path from this intermediate point to B19′. We present and compare this bilayer mechanism to other proposed and calculated mechanisms in Sec. III D. This includes calculations in which we explore the possibility of mechanisms involving a monolayer shear, shears of various thicknesses, and different martensite phases including B33. Final conclusions and acknowledgments are given in Secs. IV.

II. COMPUTATIONAL DETAILS

Density-functional electronic-structure calculations were performed using the highly precise full-potential linearized augmented plane-wave (FLAPW) method.[22] This method uses no shape approximations for the potential and charge density. The exchange-correlation contribution to the potential was included using the generalized gradient approximation within the Perdew-Burke-Ernzerhof functional[23] for all calculations. The plane-wave cutoff was set to 275 eV and the cutoff of the potential representation was set to 1,360 eV. A k-point mesh of $13\times13\times13$ was employed for all calculations which satisfied total-energy convergence to within 1.5 meV/atom for the B2 structure and 0.4 meV/atom in each of the other structures. The muffin-tin radii of Ti and Ni atoms were taken to be 2.35 and 2.10 a.u., respectively.

For a more accurate treatment of extended core electrons (i.e., Ti $3p$ electrons) that are not entirely contained within muffin-tin spheres (also known as semicore states), and which break the orthogonality between core and valence states, the method of explicit orthogonalization (XO) was used.[24] The XO approach modifies the basis of the valence states to enforce their orthogonality with the core states and so prevents the calculated valence states from having spurious core-state contributions, which could alter the character of the valence band and create so-called "ghost states," and hence have adverse effects on the accuracy of the calculated total energies. This is especially important for the correct treatment of early transition metals such as Ti, with their so-called semicore $3p$ electrons.

Structural optimization was performed for each structure for all lattice constants, angles, and internal atomic coordinates. The internal atomic coordinates were relaxed using atomic forces in geometry optimization loops prior to and following an optimization of each lattice constant and unit-cell angle which were simultaneously relaxed independently. Upon finishing the optimization of lattice constants and angles, the final atomic-coordinate relaxation caused only slight variations in the atomic coordinates with respect to their initial positions.

III. RESULTS AND DISCUSSION

A. Phase energetics and structural stability

The calculated total energies and equilibrium lattice constants of each structure of NiTi are compared in Table I and shown in Fig. 1. Shown first is the cubic B2 structure (prototype CsCl), which is the high-temperature austenitic phase.[8–10] The lattice constant for B2 was calculated to be 3.019 Å by fitting the calculated total energies versus lattice constant to the Birch-Murnaghan equation of state;[25] it is in excellent agreement with the value, 3.013 Å, obtained by Sittner *et al.*[10] with x-ray diffraction measurements. Since B2 is the high-temperature phase, we would expect it to have the highest total energy among the considered phases. This expectation is confirmed.

The next phase, R, was first identified by Goo and Sinclair[26] as having space group $P\bar{3}1m$ using convergent beam electron diffraction and transmission electron microscopy with iron-alloyed ($Ti_{50}Ni_{47}Fe_3$) samples. Hara *et al.*[11] published revisions to this structure after their electron and powder x-ray diffraction measurements indicated that the space group was $P3$ for a $Ti_{50.75}Ni_{47.75}Fe_{1.5}$ alloy. Schryvers *et al.*[12] followed these measurements using high-precision dynamic electron-diffraction experiments with the same samples and found a more symmetric structure with space group $P\bar{3}$. They attributed this to the $1a$ layer shifting up with respect to the $1c$ layer due to a combination of displacement waves in the B2→R transition. To determine the struc-

TABLE I. Structural parameters and total energies relative to the B2 structure among the different optimized structures of NiTi. Lattice constant lengths a, b, and c are given in Å. Nonright angles are stated. Volume is given in $Å^3/Z$ where Z is the number of atoms per unit cell.

Structure	Space group	Z	a	b	c	Angle (deg)	Volume	$E-E_{B2}$ (meV/atom)
			Results of this work					
B2	$Pm\bar{3}m$	1	3.019				27.516	0.00
R_1	$P3$	9	7.301		5.353	$\gamma=120$	27.452	−33.94
R_2	$P3$ [a]	9	7.299		5.359	$\gamma=120$	27.468	−33.89
R_3	$P\bar{3}$	9	7.311		5.320	$\gamma=120$	27.358	−30.78
B19	$Pcmm$	2	4.633	4.180	2.863		27.737	−40.53
B19′-109°	$P2_1/m$	2	4.707	4.159	2.933	$\beta=108.98$	27.281	−25.25
B19′	$P2_1/m$	2	4.677	4.077	2.917	$\beta=98.00$	27.541	−55.42
B33[b]	$Cmcm$	2	4.928	4.025	2.933	$\beta=107.00$	27.819	−60.07
			Experiments/previous calculations					
B2[c]	$Pm\bar{3}m$	1	3.013				27.339	
R[d]	$P3$	9	7.358		5.286	$\gamma=120$	27.533	
R[e]	$P31m$	9	7.384		5.461	$\gamma=120$	28.647	−23.00
R[f]	$P\bar{3}$	9	7.380		5.320	$\gamma=120$	27.877	
B19[g]	$Pcmm$	2	4.510	4.224	2.899		27.614	
B19′ [h]	$P2_1/m$	2	4.646	4.108	2.898	$\beta=97.78$	27.400	
B19′ [i]	$P2_1/m$	2	4.66	4.11	2.91	$\beta=98$	27.596	
B33[j]	$Cmcm$	2	5.072	4.076	3.300	$\beta=108$	32.442	
B33[k]	$P2_1/m$	2	4.951	3.993	2.953	$\beta=108.52$	32.442	

[a]This structure changed to a different space group when optimized. R_2 was taken from Gong *et al.* (Ref. 3), initially $P31m$.
[b]Initial structure taken from Huang *et al.* (Ref. 2).
[c]Experimental results by Sittner *et al.* (Ref. 10).
[d]Experimental results by Hara *et al.* (Ref. 11).
[e]Calculated results by Gong *et al.* (Ref. 3).
[f]Experimental results by Schryvers *et al.* (Ref. 12).
[g]Experimental results by Nam *et al.* (Ref. 13).
[h]Experimental results by Kudoh *et al.* (Ref. 18).
[i]Experimental results by Prokoshkin *et al.* (Ref. 17).
[j]Calculated results by Morris *et al.* (Ref. 6).
[k]Calculated results by Wagner and Windl (Ref. 4).

ture of the R phase, electronic-structure calculations were performed using the more approximate linear muffin-tin orbital (LMTO) method by Ishida *et al.*[21] with Fe additions in the unit cell to simulate the iron-alloyed structure, and found R to be of space group $P3$. Using norm-conserving pseudopotential calculations, Gong *et al.*[3] investigated several different initial configurations taken from experiment to calculate optimized lattice constants and atomic positions for equiatomic NiTi. They found the structure to be space group $P31m$.

In these iron-alloyed systems, the R phase is the martensite product phase. However, the R structure is also an intermediate phase in equiatomic and near-equiatomic NiTi; thus, to reconcile these ambiguities, we performed FLAPW calcu-

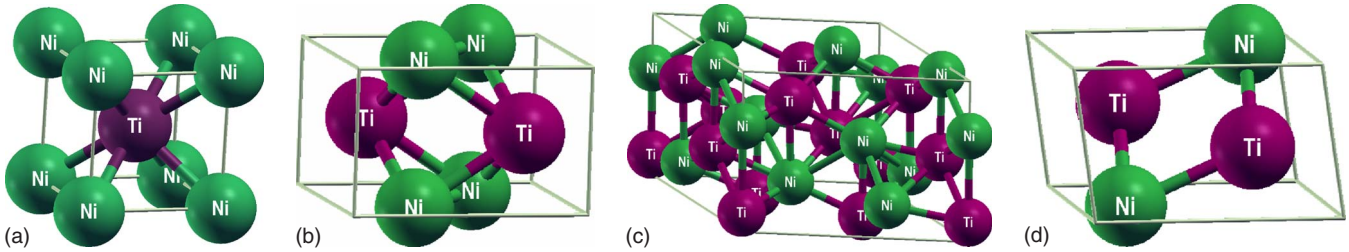

FIG. 1. (Color online) The observed experimental structures of NiTi: (a) B2, (b) B19, (c) R, and (d) B19′.

TABLE II. Internal coordinates of initial and final R structures. The multiplicity and Wyckoff letters are given under "Site."

	Initial				Final			
Atom	Site	x	y	z	Site	x	y	z
Space group			$P3$				$P3$	
Ti	1a	0	0	0	1a	0	0	0
Ti	1b	1/3	−1/3	0.151	1b	1/3	−1/3	0.100
Ti	1c	−1/3	1/3	0	1c	−1/3	1/3	−0.002
Ti	3c	0.333	−0.019	0.416	3c	0.333	−0.010	0.390
Ti	3c	0.692	0.025	0.708	3c	0.672	0.006	0.691
Ni	1a	0	0	0.507	1a	0	0	0.466
Ni	1b	1/3	−1/3	0.65	1b	1/3	−1/3	0.637
Ni	1c	−1/3	1/3	0.506	1c	−1/3	1/3	0.464
Ni	3c	0.333	−0.022	0.913	3c	0.333	−0.023	0.909
Ni	3c	0.667	0.014	0.211	3c	0.692	0.026	0.183
Space group			$P31m$				$P3$	
Ti	1a	0	0	0	1a	0	0	0
Ti	2b	1/3	−1/3	−0.09	1b	1/3	−1/3	0.102
Ti		−1/3	1/3	0.09	1c	−1/3	1/3	−0.005
Ti	3d	0.342	0	0.397	3c	0.333	−0.010	0.391
Ti	3d	0.678	0	0.701	3c	0.678	0.006	0.690
Ni	1a	0	0	0.507	1a	0	0	0.462
Ni	2b	1/3	−1/3	−0.377	1b	1/3	−1/3	0.641
Ni		−1/3	1/3	0.377	1c	−1/3	1/3	0.459
Ni	3d	0.362	0	0.905	3c	0.333	−0.023	0.911
Ni	3d	0.684	0	0.182	3c	0.688	0.026	0.181
Space group			$P\bar{3}$				$P\bar{3}$	
Ti	1a	0	0	0	1a	0	0	0
Ti	2d	1/3	−1/3	−0.09	2d	1/3	−1/3	−0.043
Ti	6g	0.322	0	0.299	6g	0.341	0.331	0.345
Ni	1b	0	0	0.507	1b	0	0	1/2
Ni	2d	1/3	−1/3	0.377	2d	1/3	−1/3	0.419
Ni	6g	0.316	0	0.818	6g	0.340	0.315	0.859

lations to determine the symmetry and atomic configuration of the equiatomic NiTi R phase. This phase is more difficult to measure experimentally in equiatomic NiTi since it exists as an intermediary between the austenite and martensite phases and, depending on conditions of the sample, does not necessarily form at all. Thus, we structurally optimized each input configuration, namely, the experimental structures from Schryvers *et al.*,[12] with space group $P\bar{3}$, from Hara *et al.*,[11] with space group $P3$, and a theoretical structure proposed by Gong *et al.*,[3] with space group $P31m$, to determine the correct symmetry of the R structure. After performing geometry and unit-cell optimization cycles, we compared total energies and atomic structures. Detailed results of atomic position changes are shown in Table II.

Our optimization of Hara's experimental configuration resulted in a slight reordering of the z components of the atomic positions, an expansion of the c lattice constant by 1.3% (from 5.286 to 5.353 Å) and a contraction of the a lattice constant by 0.8% (from 7.358 to 7.301 Å). The final calculated structure was space group $P3$. Our optimization of Gong's calculated structure, however, lowered the symmetry of the $P31m$ structure and again $P3$ resulted; during this optimization, the input symmetry is broken as atoms at Wyckoff position 2b move to occupy positions 1b and 1c with small shifts in the z components of the atomic positions. In addition, the lattice constants a and c contracted by 1.2% and 1.9%, respectively. As a result of these optimizations, the two final $P3$ structures have identical lattice constants (within 0.1%), total energies that differ by only 0.05 meV/atom, and atomic coordinates which are nearly identical but differ by at most 0.3 Å which is likely due to small computational round-off errors.

The $P\bar{3}$ structure measured by Schryvers *et al.* did not change symmetry during our optimization; there were lateral shifts of the 6g Wyckoff positions and slight shifts in the z coordinate of each atom. While this structure is more sym-

metric, the calculated total energy was 3 meV/atom higher than the total energy of the R structures with space group $P3$. While very small, these total-energy differences still imply that the $P\bar{3}$ structure is less stable than the $P3$ one. Each of the R phases are around 30–34 meV/atom lower than B2, showing both that the R phase would be formed at slightly higher temperatures than the B19 phase and that it is less stable than B19′ or B33. Thus, our findings that show the R structure of equiatomic NiTi to be space group $P3$ agree with calculations by Ishida and the first major revisions to the structure by Hara. Since the total-energy differences between the $P3$ and the $P\bar{3}$ structures are small, it is reasonable to conclude that slight Fe additions such as in samples used by Schryvers *et al.* with 1.5% iron, could change the symmetry of the structure to $P\bar{3}$.

Now, the B19 phase is an intermediate orthorhombic phase in the B2→B19′ transformation when NiTi is alloyed with Cu. Additionally, in several binary and ternary shape-memory alloys such as TiPd, TiNiPd, TiNiPt, and TiAu,[15,16,27] B19 is the martensitic phase of the shape-memory transformation. A striking difference between these materials is the martensitic transformation temperature. TiNiPt thin films and bulk TiAu exhibit a martensitic transformation to B19 at 627 K (Ref. 16) and 875 K,[27] respectively, whereas the transformation temperature for NiTi to B19 is 343 K, i.e., much closer to room temperature. We seek to understand why these differences occur among shape-memory alloys.

The B19 phase is experimentally observed[13,14] as an intermediate phase in NiTi alloyed with 7.5–20 % of copper. For alloys with more than 20% copper, B19 is the martensitic phase.[13] We determined the energetics, stability, and crystal structure of B19 using equiatomic NiTi. Calculations of the unit-cell deformations yielded results that are close to experiment,[13] overestimating a by 2.7% and underestimating b and c by 1.1% and 1.2%, respectively, and changes to the internal coordinates were negligible with geometry optimization. Elastic properties displaying the stability of this structure will be examined in Sec. III B; its total energy is 41 meV/atom below B2, indicating that this structure is likely formed at higher temperatures than the B19′ or B33 structures and is less stable than these structures in the equiatomic case. This is reflected in NiTi ternary alloys for which B19 is the martensite; they often have higher martensitic transformation temperatures.

The B19′ structure, first proposed by Hehemann and Sandrock,[28] has been heavily studied both experimentally and theoretically.[8,9,18,19] Recently, Prokoshkin *et al.*[17] performed x-ray diffraction measurements at a range of temperatures with different Ti compositions, ranging from 47% to 50.7%. Our calculations agree with their experimental lattice constants and atomic positions to within 1% for equiatomic NiTi. As found previously for density-functional-theory calculations (simulating $T=0$ behavior), which simultaneously optimize all structural and internal coordinates,[2,4,5] this structure has an instability to monoclinic angle relaxation. Thus, the monoclinic angle was fixed to 98°. The differences in our calculations with respect to the equiatomic results of Prokoshkin *et al.* are as follows; we overestimated the a and c lattice constants by around 0.3%, and we underestimated b by 0.8%.

The B19′ phase had been well established as the low-temperature martensitic phase by experiment and theory until the paper by Huang *et al.*,[2] who proposed a BCO structure as a martensitic phase and suggested that the observed B19′ is stabilized by internal stresses. Morris *et al.*[6] subsequently calculated a transformation from B2 to this phase, which they identified as B33. Later, Wagner and Windl[4] calculated elastic properties of this phase and verified its stability. They also examined the stresses required to stabilize the B19′ structure from B33 and determined that the pressures amounted to only around 1 GPa.

Given these findings and the lack of experimental verification of this phase, it is increasingly important to check the predictions of *ab initio* calculations. Here, we examine the problem using the FLAPW method as opposed to pseudopotential[2,4] or projector-augmented wave methods[4] used previously. Using the structure found in Ref. 2, we optimized all lattice constants, angles, and internal coordinates, and calculated a total energy that was indeed lower than the B19′ structure by 4.65 meV/atom. All lattice constants were within 1% of those previously reported. In previous calculations,[2,4] the B33 phase was calculated to have a lower energy than B19′. We confirm this result. In addition, there are many similarities between the B19′ phase and the calculated B33 phase; the lengths of the lattice constants of B33 and B19′ are nearly identical (with the exception of the a lattice constant which is elongated by 5% for the B33 phase) so the primary difference is the monoclinic angle which is 107° and 98°, respectively. As for energetics, these phases have definitively lower energies than every other identified phase. Thus, these phases' attributes are exceedingly similar.

The symmetry of this structure has also been a matter of dispute. As noted in Ref. 2, the higher-order symmetry space group $Cmcm$, must meet two criteria reported in the above form $\cos\beta = a/2b$ and $4x_m - 1 = 2y_m$, where x_m and y_m are the internal x and y coordinates of Ni or Ti, and β is the monoclinic angle. Our optimized internal coordinates of (0.357,0.212,1/4) and (0.084,0.331,1/4) and reported structural parameters, the monoclinic angle of 107° and lattice lengths in Table I, satisfy these criteria. A slightly larger monoclinic angle of around 108° was found in other previous calculations,[4,6] which we believe is due to differences in computational parameters such as the density of the k-point mesh. The stability of B33 will be further examined in Sec. III B.

Measured changes in enthalpy near the arrest temperature of NiTi have been attributed to features of the shape-memory effect.[29] Thus, a clear picture of formation energy differences among the phases can clarify shape-memory behavior, and while formation energies are often difficult to measure experimentally, they are very important in understanding transformation mechanisms and barriers. In Table III, we present calculated austenitic, martensitic, and intermediate phase formation energies of NiTi and compare them with previous experiments and theoretical calculations. The formation energy is calculated from the total energy of B2 NiTi and the total energies of elemental Ni and Ti in their corresponding lowest-energy phases, namely, fcc Ni and hcp Ti, as ΔE_{form}

TABLE III. The formation energies (of the B2 phase except where noted otherwise) for NiTi.

Reference	Formation energy (kJ/mol atom)
Experiment[a]	−33.9
Experiment[b]	−34.0
FP-LMTO calculation[c]	−38.0
FP-LMTO calculation[d]	−36.0
This work (FLAPW)	
B2	−34.1
R	−37.4
B19	−38.0
B19′	−39.5
B33	−39.9

[a]Reference 30.
[b]Reference 31.
[c]Reference 19.
[d]Reference 32.

$=E_{\mathrm{NiTi}}^{\mathrm{B2}}-(E_{\mathrm{Ni}}^{fcc}+E_{\mathrm{Ti}}^{hcp})$. Lattice constants for each structure and the a/c ratio for hcp Ti were optimized. Fcc Ni was treated in a spin-polarized regime and the calculated magnetic moment for Ni is $0.63\mu_B$. Using these structures, we obtained a formation energy of −34.1 kJ/mol atom. Experimental direct reaction calorimetry measurements made by Gachon *et al.*[30] and Kubaschewski[31] recorded values of −33.9 kJ/mol atom and −34.0 kJ/mol atom, respectively, each of which have a standard deviation of 2 kJ/mol atom. Our results agree with experiment within 0.2 kJ/mol atom to these values and are in much better agreement than previous calculations. Additionally, we have provided formation energies for other phases; R, B19, B19′, and B33 which are formed 3.3, 3.9, 5.4, and 5.8 kJ/mol atom below B2, respectively.

B. Elastic constants

Indications of brittle versus ductile behavior, plastic response to deformation, and precursor phenomena in the martensitic transformation may be garnered from a detailed investigation of NiTi's elastic constants. Despite having a complex polycrystalline structure, both bulk and single-crystal properties may be examined by means of precise first-principles calculations. To date, the elastic constants of NiTi have been studied both experimentally and theoretically but not all elastic constants have been reported for all phases.[4,5,7,33,34] In fact, until recently,[4] individual experimental and theoretical elastic constants had only been reported for the B2 phase of NiTi. Thus, we have calculated the elastic constants for each of the intermediate, martensitic, and austenitic structures since their experimental determination can be difficult with a material that goes through a structural change with applied pressures. These results are presented in Table IV.

The experimental measurements of elastic constants of the B2 phase of NiTi were performed by Mercier *et al.*[34] at 298 K, the lowest temperature at which the B2 phase is stable. Brill *et al.*[33] measured the B2 elastic constants at 400 K. The comparison between these two experiments shows

TABLE IV. Calculated and experimental independent elastic constants for NiTi structures (in GPa; except A, dimensionless).

	B2	B2[a]	B2[b]	B2[c]	B2[d]	B19	B19[c]	R ($P3$)	R ($P\bar{3}$)	R ($P3_1/m$)	B33	B33[c]	B19′	B19′ [c]
C_{11}	183	137	162	138	204	192	212	245	245	248	249	226	249	223
C_{12}	146	120	129	169	134	105	129	111	109	113	133	137	129	129
C_{13}						150	92	117	121	124	99	113	107	99
C_{15}											27	33	15	27
C_{22}						254	238				232	231	245	241
C_{23}						118	127				131	134	125	125
C_{25}											−15	1	−3	−9
C_{33}						240	203	221	214	215	189	179	212	200
C_{35}											−11	−18	−1	4
C_{44}	46	34	34	40	53	66	65	51	51	51	99	84	87	76
C_{46}											4	2	−4	−4
C_{55}						73	−32				44	23	66	21
C_{66}						53	49				96	90	86	77
B	159	126	142	159	157	156	150	155	155	159	156	156	159	152
C' [e]	19	9	17	−16	35	33	47	58	54	54	40	36	52	48
A	2.49	4.00	2.06	−2.58	1.51	1.60	−0.68	0.87	0.94	0.95	1.11	0.65	1.27	0.44

[a]Experiment at 400 K (Ref. 33).
[b]Experiment at 298 K (Ref. 34).
[c]Calculated results by Wagner and Windl (Ref. 4).
[d]Calculated results by Hu *et al.* (Ref. 35).
[e]C' is calculated differently depending on the symmetry of the structure (see Appendix).

that the values of C_{11}, C_{12}, C', and B decrease with respect to increasing temperature. We therefore use Mercier's data to compare with our results. In comparison, our calculated values of C_{11}, C_{12}, and C_{44} are overestimated by 14%, 14%, and 35%, respectively. The bulk modulus (B), the Zener anisotropy (A), and C' are overestimated by 10%, 19%, and 12%. Since DFT calculations simulate ground-state properties of a material at 0 K, no temperature effects or lattice vibrations are taken into account. Considering that elastic constants usually decrease with temperature, the discrepancies with experiment are likely due to omissions of temperature effects.

Although there is abundant need for single-crystal elastic constants for all phases of NiTi, no reliable experimental data exists and only recently have theoretical calculations begun to appear for any intermediate and martensitic phases. An extensive study of the elastic properties of NiTi was recently completed by Wagner and Windl,[4] in which they calculated the elastic constants of B19, B19′, and B33 using pseudopotential methods. Our FLAPW method calculations are compared with their reported values in Table IV, and the R-phase elastic constants are reported. While there is considerable agreement between these calculations and a similar formalism was used to obtain these results (see Appendix and Ref. 4 for details), we note two primary methodological differences. First, we did not allow internal coordinate or stress-tensor optimization at each lattice distortion. Since lattice distortions were small (up to 2%), this constraint may preserve metastable states, mimicking the entropically stabilized high-temperature effects. Second, because each state was metastable, no stress controls were imposed for any of the elastic-constant calculations.

Due to these differences, there are three large discrepancies between these sets of results. First, we find C_{12} to be lower than C_{11} for the B2 phase of NiTi, yielding a positive C' value which gives a metastable B2 structure versus Wagner and Windl who calculated a negative B2 C' of −16 GPa. Second, the C_{55} elastic constant of the B19 phase is positive whereas they reported a negative C_{55} value. Third, our B19′ C_{55} elastic constant is three times their obtained result. While the results of Wagner and Windl would explain the susceptibility of the B2 phase to tetragonal distortion and the B19 and B19′ phases to monoclinic distortions, by not relaxing the internal coordinates we can learn more about the properties of the entropically stabilized metastable states. Indeed, their C' is quantitatively lower than the present results and other calculated values, such as those of Hu *et al.*[35] in which a screened Korringa-Kohn-Rostoker method was employed. Additionally, their C' is fully unstable which qualitatively contradicts experiment. Thus, we find that our FLAPW results have a higher accuracy in calculating both of these constants. The consistency of our results leads us to conclude that our calculations and methodology accurately predict experimental measurements, capturing both major qualitative features and accurate quantitative results.

Given the agreement with experiment, we now calculate and compare single-crystal and macroscopic moduli for each structure of NiTi. The most pronounced effect is the increase in rigidity of C' (see Table IV) and C_{44} from the B2 phase to each other phase. Between B2 and B19′, the increase in C_{44} is almost twofold and takes two large steps; first, increasing by 50% to B19 then again by the same amount to B19′. While the utility of C' as an indicator of stability is not clear, our calculations indicate that it increases by a factor of 3, when compared to the R phase, and to a factor of 2–3, when compared to B19, B33, and B19′. Thus, given that C_{44} and C' are much lower for B2 than for the other phases, this would suggest that the softening of these values in B2 allows the high-temperature state to deform into more complex phases as the temperature is decreased. Indeed, soft C_{44} and C' have previously been linked to instabilities in the B2 phase and its transformation to martensite.[36] However, the Zener anisotropy, A, decreased from B2 to each other phase. This supports the experimental findings of Brill *et al.*,[33] which show a sharp decrease in the anisotropy factor at the martensitic transition temperature.

As with C' and the Zener anisotropy, single-crystal elastic constants yield insights into the ductility, stability, and phase formation of polycrystalline martensitic materials. So while first-principles calculations are limited to periodic single-crystal behavior and bulk NiTi does not form single crystals, instead forming complex structures which include anisotropic precipitates and polycrystalline domains with intricate grain and twin boundaries, we may still extrapolate useful theoretical macroscopic elastic properties that find good agreement with experiment.

Thus, we examine the polycrystalline bulk (B), shear (G), and Young's (E) moduli, and Poisson's ratio (ν) using the Voigt and Reuss moduli (denoted with subscripts V and R) with Hill averaging (no subscripts) and present these results in Table V along with experimental and theoretical comparisons (refer to the Appendix for details). As with the reported B2 elastic constants, there is strong agreement between the current calculated results and the elastic properties calculated from experimental elastic constants for the B2 phase, and our results compare favorably with previously reported theoretical results. We note that Wagner and Windl applied an elastic-constant method that yielded a fully unstable B2 phase. Thus, B2 macroscopic elastic parameters calculated from their elastic constants are not applicable to a stable B2 phase. Our calculations will be compared with their reported results for B19′ and B33 as those phases either metastable or stable. We also note that our differences between the Voigt and Reuss methods are much smaller than found by Wagner and Windl, and yield more precise elastic properties.

By comparing the elastic properties of these phases, several trends appear. First while the bulk modulus remains fairly constant among phases, the shear modulus increases greatly from B2 to other phases. B19′ exhibits the highest shear modulus, resisting further shear as B2 is transformed. Notably, B19′ has a higher shear modulus than every other phase, including B33.

Second, Pugh's empirical rule has been used to link plastic behavior to low G/B ratios for both pure metals and intermetallics.[35,37] Materials exhibiting a G/B ratio less than 0.57 are more likely to be ductile. All of the NiTi structures satisfy this highly empirical criterion showing intrinsic ductility; yet given its low shear modulus, this rule may be exaggerated for B2 due to high anisotropy and plane-dependent differences in shearing behavior. This will be examined in Sec. III C and the origin of this discrepancy will be identified.

TABLE V. Calculated macroscopic elastic properties for NiTi structures (GPa; except A, G/B, and ν, dimensionless).

	B2	B2[a]	B2[b]	B2[c]	B19	R ($P3$)	R ($P\bar{3}$)	R ($P3_1/m$)	B33	B33[b]	B19′	B19′ [b]
A	2.49	2.06	−2.58	1.51	1.6	0.87	0.94	0.95	1.11	0.65	1.27	0.44
$A^{-1/2}$	0.63	0.70	N/A	0.81	0.79	1.07	1.03	1.02	0.95	1.24	0.89	1.51
B_V	158	140	159	157	159	156	156	159	155	156	159	152
B_R	159	140	−17	158	156	155	155	158	151	151	157	142
G_V	35	27	18	46	59	58	58	58	68	56	71	56
G_R	29	24	−453	44	54	57	56	56	53	22	67	34
B	159	140	71	158	157	156	156	159	153	154	158	147
G	32	25	−218	45	57	58	57	57	60	39	69	45
ν	0.41	0.41	1.77	0.37	0.34	0.34	0.34	0.34	0.33	0.38	0.31	0.37
G/B	0.20	0.18	−1.37	0.29	0.36	0.37	0.37	0.36	0.39	0.25	0.43	0.30
E_V	98	76	51	125	158	155	154	154	179	151	184	149
E_R	82	68	−139	121	145	153	151	150	141	63	176	95
E	90	72	−44	123	151	154	152	152	160	107	180	122

[a]From experimental elastic constants (Ref. 34).
[b]From calculated results by Wagner and Windl (Ref. 4).
[c]Calculated results by Hu *et al.* (Ref. 35).

Third, another empirical criterion for plastic response to deformation requires the Poisson's ratio and the anisotropy factor to satisfy certain conditions. From examining brittle and ductile behavior in intermetallic, elemental, and ionic compounds, Gschneidner *et al.*[38] proposed that B2 intermetallics achieve ductility when having an anisotropy factor greater than 0.8 and a Poisson's ratio less than 0.35. In previous calculations, Hu *et al.*[35] proposed that NiTi was near this range and thus would exhibit some amount of ductility. However, our calculated values for B2 NiTi are clearly outside of this range with a Poisson's ratio of 0.41 and an anisotropy factor of 0.63. Furthermore, when compared with B2, ν is higher and $A^{-1/2}$ is lower for each other phase such that ν and $A^{-1/2}$ are within the range for ductile behavior for the B19′, R, and the proposed B33 phases. Thus, B2 NiTi is not intrinsically ductile despite meeting Pugh's empirical rule. Instead, B2 relies on polycrystalline effects and martensitic behavior to allow macroscopic ductility.

Lastly, the Muller-Achenbach-Seelecke model,[39] which requires the Young's modulus of the austenite, E_A, be smaller than that of the martensite, E_M, was upheld by previous calculations.[4] Here, we too find that this model is confirmed with E_A(90 GPa) substantially smaller than E_M(180 GPa). Note also that B19′ again marks an extremum for yet another elastic parameter while the Young's modulus of the B19 and R phases lie in between these values. Additionally, these Young's moduli may be directly compared with experiment. Rajagoplan *et al.*[40] measured macroscopic Young's moduli of NiTi to be between 101 and 162 GPa using indentation experiments. This agrees with our *ab initio* elastic constants of the B2 and B19′ phases to within 12% and 11%, respectively.

Since calculated R-phase elastic properties have not been reported elsewhere, we comment briefly on some of their features. First, the elastic constants do not vary greatly among the different symmetries as one would expect given the previously discussed structural similarities. These phases have the highest C' elastic moduli of the phases, nearly the same but slightly greater than B19′ and high anisotropy factors, and so they appear resistant to crystal strains. However, the shear modulus, the G/B ratio, and the Young's modulus lie squarely between B2 and B19′ extremums, yielding expected properties for an intermediate phase of the transformation path.

To conclude, we have calculated accurate elastic properties and obtained both individual elastic constants and macroscopic elastic parameters. Since the two empirical ductility criteria give opposing results for the B2 phase, we conclude that it is not intrinsically ductile. Instead, ductility in NiTi is created through its polycrystalline composition and martensitic behavior. Namely, the B19′ phase is more intrinsically ductile than B2; thus, it acts as a barrier to creep and crack formation. Additionally, due to its higher shear modulus, B19′ is stabilized by internal stresses whereas the B33 phase is unstable in a stressed environment.

C. Generalized stacking-fault energetics

Generalized stacking-fault (GSF) energetics,[41] also referred to as γ surfaces, give insight into the ductility, dislocation mobility, and crack blunting in materials. First-principles shear energetics have been well studied in such B2 binary alloys as NiAl and FeAl.[42] GSF energy, $E_{GSF}(u)$, is defined as the energy associated with a rigid shift of one half of an ideal infinite crystal with respect to another half of an arbitrary fault vector, u, on a certain slip plane. In practical calculations, the infinite crystal is approximated with a supercell of a sufficient thickness to eliminate interactions between slip-plane images.

We performed γ-surface calculations on B2 NiTi by similarly distorting a supercell of NiTi with a rigid shift along the {001}, {011}, and {111} slip planes. We calculated the total energies at intervals of $0.1a$ in the two dimensions parallel to the slip plane, where a is the B2 lattice constant. Initially, the

TABLE VI. Energy barriers and unstable stacking-fault energies.

		Unrelaxed barrier		Relaxed barrier	
Plane	Layers (thickness) (Å)	Direction	Height (J/m^2)	Direction	Height (J/m^2)
(001)	2(3.0)	⟨100⟩	2.08	⟨100⟩	1.22
	3(4.5)	⟨100⟩	2.10	⟨100⟩	1.28
	4(6.0)	⟨100⟩	2.14	⟨100⟩	1.09
	6(9.1)	⟨100⟩	2.09	⟨100⟩	1.10
(011)	2(4.3)	⟨111⟩	1.39	⟨100⟩	0.31(0.12)[a]
	3(6.4)	⟨111⟩	1.26	⟨100⟩	0.47(0.38)
	4(8.5)	⟨111⟩	0.89	⟨100⟩	0.13(0.11)
	6(12.8)	⟨111⟩	1.06	⟨100⟩	0.11
(111)	3(2.6)	$\langle\bar{2}11\rangle$	0.76[b]	$\langle\bar{2}11\rangle$	0.53[b]
	4(3.5)	$\langle\bar{2}11\rangle$	1.34	$\langle\bar{2}11\rangle$	1.09
	6(5.2)	$\langle\bar{2}11\rangle$	0.88	$\langle\bar{2}11\rangle$	0.62

[a]Stable stacking fault.

[b]All unrelaxed and relaxed (111) barriers are taken at $\frac{1}{6}\frac{u}{a}$ in the $\langle\bar{2}11\rangle$ direction.

maximum thickness of the supercell was chosen to ensure that periodic effects due to the shearing at the slip plane disappeared within the layers. To examine possible atomistic mechanisms to martensitic transformation, this was slowly reduced to thinner slabs in order to find a minimum-energy barrier. For the {001} slip plane, the unit cell was chosen with axes a, $b=a$, and $c=2a,3a,4a$, or $6a$. Thus, the supercell is two to six atomic layers thick between each slip plane. For {011} slip, the unit cell was chosen with axes a, $b=\sqrt{2}a$, and $c=\sqrt{2}a,3/2\sqrt{2},2\sqrt{2}a,3\sqrt{2}a$, with thicknesses of two to six atomic layers. For {111}-planar stacking-fault calculations, the unit cell is set as hcp with $a_{111}=\sqrt{2}a$ and $c=\sqrt{6}a_{111}/6,\sqrt{6}a_{111}/4,\sqrt{6}a_{111}/3,\sqrt{6}a_{111}/2$. Thicknesses are two to six atomic layers and packing is much tighter (see Table VI). For approaching Ni and Ti atoms, muffin-tin radii were reduced to the maximum value without an overlap.

First, total energies were calculated for a set of shear vectors. Then, the full γ surface for an arbitrary fault vector was constructed using a Fourier expansion over K_n vectors reciprocal to the slip vectors such that

$$E_{\mathrm{GSF}}(u)=\sum_{n=1} C_n[1-\cos(K_n u)], \tag{1}$$

where $K_n u=n_1k_1+n_2k_2$, $k_1=(2\pi/a)$, and $k_2=(2\pi/b)$ for each slip plane, n_1 and n_2 are integers, and the C_n are determined with a mean least-squares fit to the calculated energies. Next, we relaxed each structure in order to determine the preferred atomic locations along the slip plane, relaxing the atomic coordinates throughout the stacking fault. This resulted in significant movement of the atomic coordinates and greatly affected the total energies throughout the γ surface.

Calculations of the {001} γ surface showed a high-energy barrier to shear in all directions (see Fig. 2 and Table VI). In addition, to complete the rigid shift to half of a lattice constant in the ⟨110⟩ direction, the muffin-tin radii for overlapping atoms had to be reduced so drastically that the high electron loss from the core electrons within the muffin tins made it impossible to obtain meaningful total energies. In the ⟨100⟩ direction, sizable unstable stacking-fault barriers of over 2 J/m^2 were recorded. This is comparable with the unrelaxed value of 3.3 J/m^2 in NiAl.[42] These barriers were reduced to nearly half their original size by employing atomic relaxation, yet barriers remained large and greater than 1 J/m^2. These results were essentially identical for different slab thicknesses showing that the topology and the barrier heights are not heavily affected by changes in the number of layers but B2 NiTi is highly resistant to {001} shear. Thus, this slip is unlikely to be a primary mechanism to diffusionless shear and does not accommodate creep.

Rigid shifts in the {011} planes were successful throughout the γ surface. Figure 3 shows the energy versus shear along the {011} slip plane. For all thicknesses examined, the lowest-energy barrier of the nonrelaxed γ surface is in the ⟨111⟩ direction and the barrier height is less than 1.4 J/m^2 and varies depending on the slab thickness. These unrelaxed unstable stacking-fault barriers are around 2/3 to 2/5 of those in the {001} plane and are even lower than relaxed {001} energy barriers. Next, we employ geometry optimization for the {011} γ surface which greatly affects its topology. This atomic relaxation significantly reduces the energy surface along the ⟨100⟩ direction, revealing a minimum-energy shear path. Additionally, stable stacking-fault barriers emerge for thicknesses of two, three, and four layers, and while all energy barriers are very small, unstable stacking-fault barriers are slightly higher for the four-layer case and nearly three times higher for the two-layer case. Yet at the edge of the γ surface, the energy barriers are approximately 0.1 J/m^2 for the two-, four-, and six-layer cases (the three-layer case has a barrier of 0.38 J/m^2 here). Thus, for these thicknesses, B2 NiTi is susceptible to stacking faults along the {011} plane, which is facilitated by atomic relaxation, revealing low-energy barriers in the ⟨100⟩ direction.

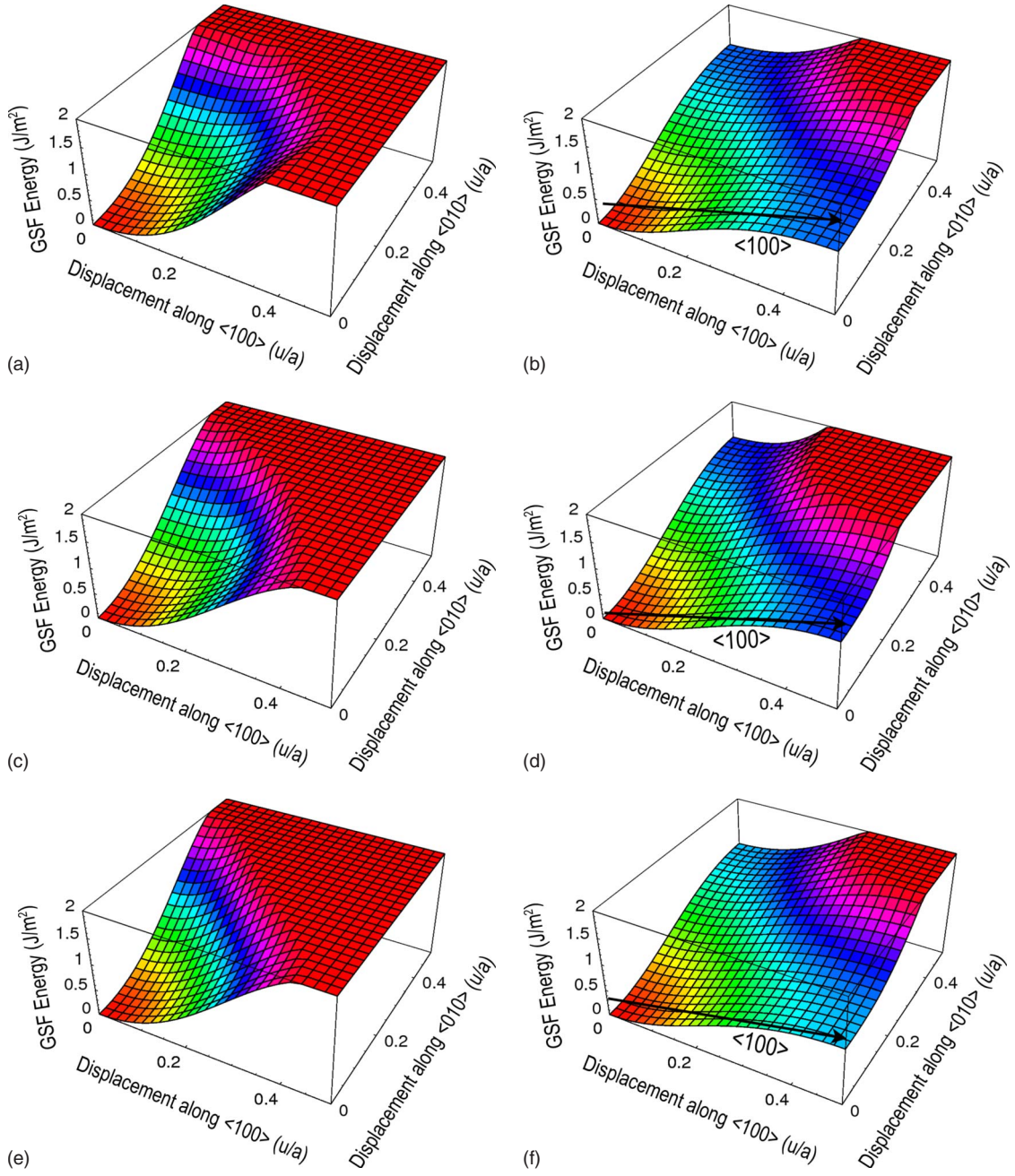

FIG. 2. (Color online) The γ surfaces in the {001} slip plane for B2 NiTi for two layers {(a) and (b)}, three layers {(c) and (d)}, and four layers {(e) and (f)} (a cutoff of 2 J/m^2 is imposed). For (a), (c), and (e) no relaxation was employed. For (b), (d), and (f), atomic coordinates were relaxed.

The slab thickness of {011} planes more clearly affects the topology of the surfaces than for {001} shear. The two- and three-layer slabs have greater resistance to ⟨011⟩ shear for both unrelaxed and relaxed calculations. After relaxation, small unstable energy barriers remain at around $0.3\frac{u}{a}\langle 100\rangle$ for these thicknesses. The three-layer case is clearly not preferred given that the stable stacking-fault barrier is more than three times higher than at other thicknesses. However, the two-layers case is unique in that it exhibits a stable stacking fault that is approximately 1/3 the size of its unstable stacking-fault barrier, and nearly the same height at the edge of the γ surface as for the thicker layers. Additionally, relaxation reduces its energy barriers by the greatest margin as small atomic movements sharply affect total energies. Therefore, while there is a sizable unstable stacking-fault barrier to two-layer shear, some other slight deformation of the lattice such as Bain-strain distorting lattice constants, may further accommodate this shear, enabling bilayer faults to occur with negligible energy barriers. This will be further examined in Sec. III D with respect to the transformation path.

Many alloys of NiTi transform to an R phase before transforming to the martensitic structure. For NiTi, this phase is based on an hcp symmetry, as shown in Table I. The shearing mechanism which most likely leads to this phase's formation

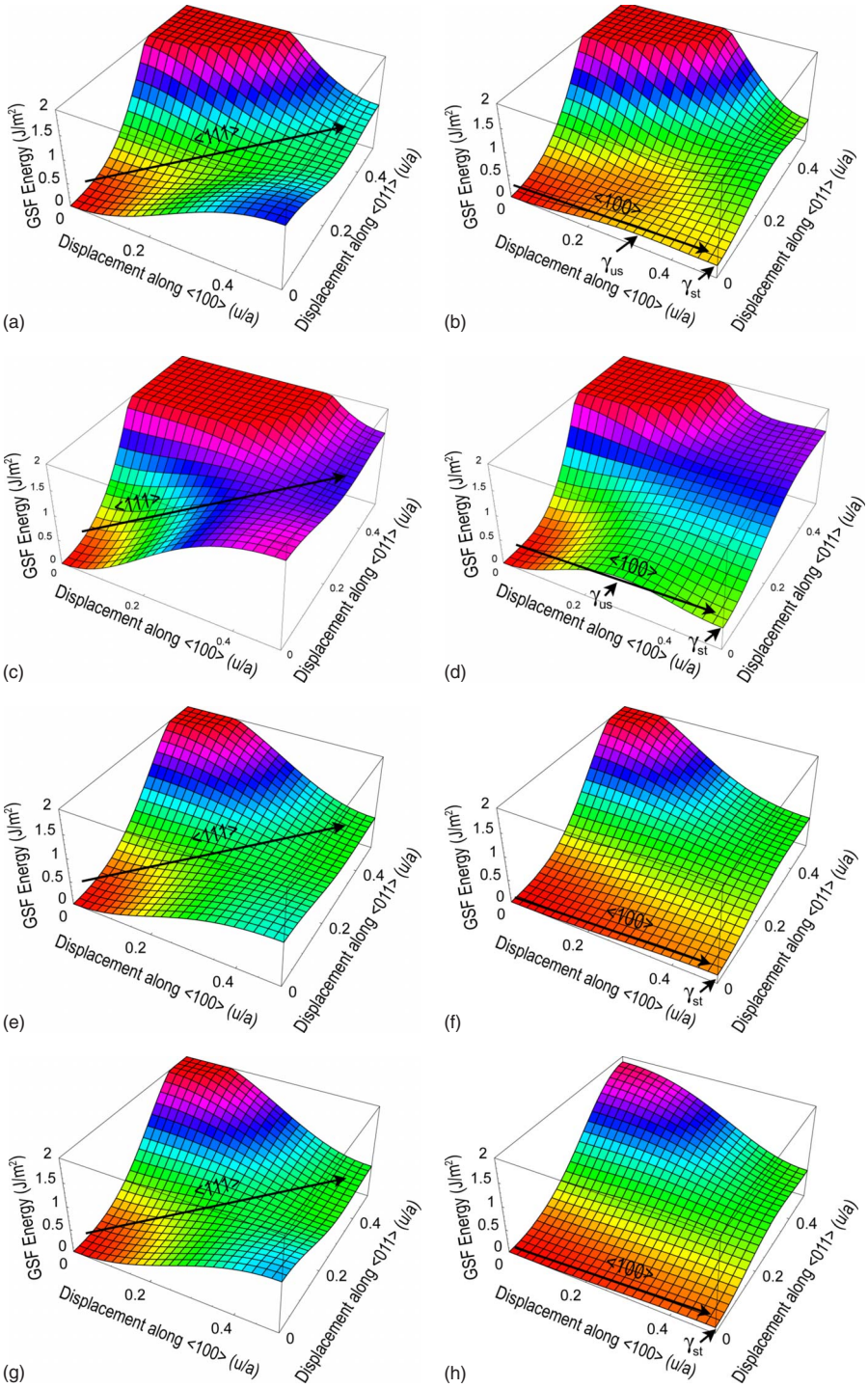

FIG. 3. (Color online) The γ surface in the {011} slip plane for B2 NiTi for two layers {(a) and (b)}, three layers {(c) and (d)}, four layers {(e) and (f)}, and six layers {(g) and (h)} (a cutoff of 2 $\mathrm{J/m^2}$ is imposed). For (a), (c), (e), and (g) no relaxation was employed. For (b), (d), (f), and (h), atomic coordinates were relaxed.

is due to {111} shear, which we calculate and show in Figs. 4 and 5. These stacking faults have very high barriers, beyond $0.2a$ in all directions, with the unstable stacking fault occurring at $(\frac{1}{3}a,0)$, $(0,\frac{1}{3}a)$, and $(\frac{1}{3}a,\frac{1}{3}a)$. Near this unstable stacking fault, as in the $\langle 110\rangle\{001\}$ fault, it was impossible to calculate meaningful total energies. This gap occurs in the $\langle \bar{1}10\rangle$ and $\langle \bar{2}11\rangle$ directions between $0.2\frac{u}{a}$ and $0.8\frac{u}{a}$ for all slab thicknesses.

As in the {011} γ surface, there are major topological differences in each surface depending on the number of layers that are used. As stated above, given the impossibility of shearing toward the unstable stacking fault due to atomic overlap, we could not obtain meaningful values for the energy barriers. So, we used a constant reference point of $(\frac{1}{6}a,\frac{1}{6}a)$ to compare shear energies (see Table VI). Layers divisible by 3 (three and six layers) have lower barriers, un-

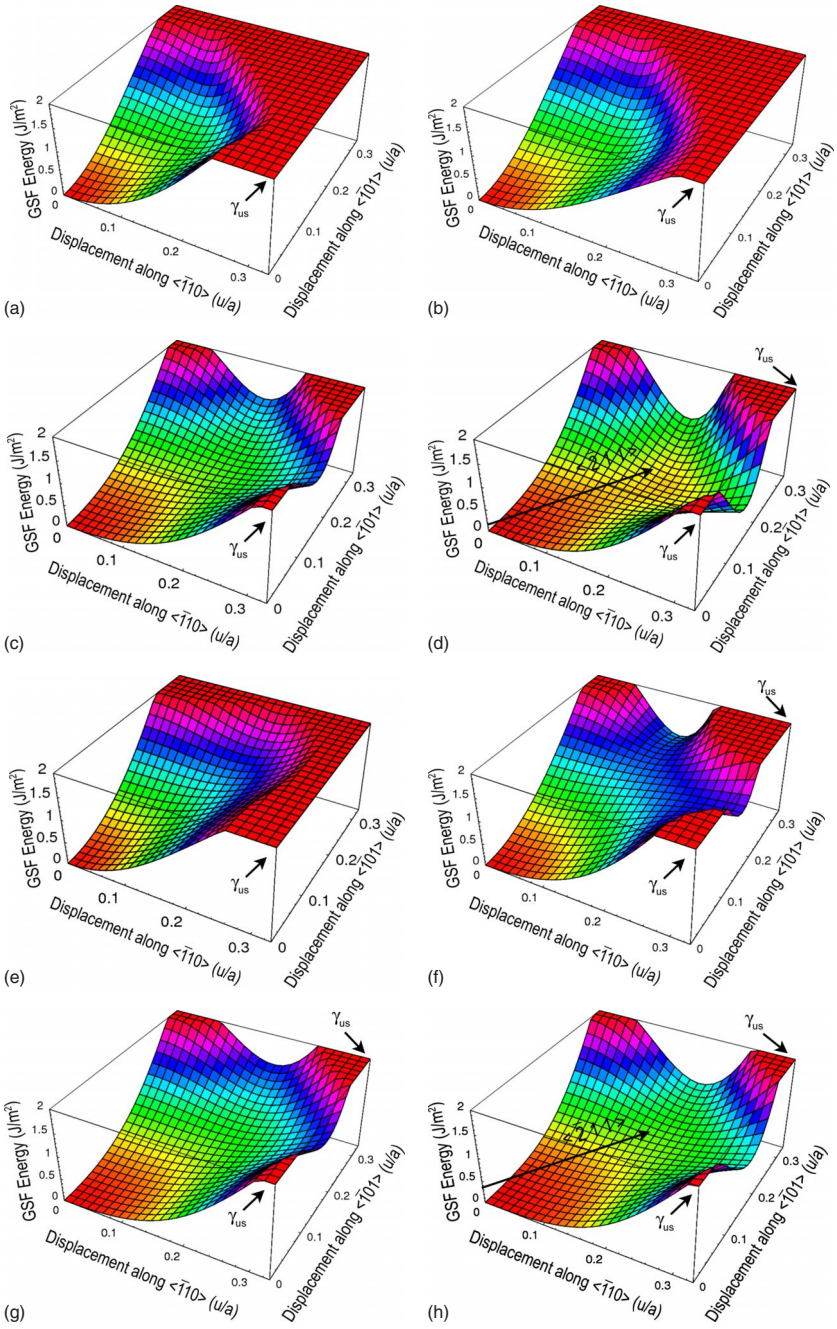

FIG. 4. (Color online) The γ surface in the {111} slip plane for B2 NiTi for two layers {(a) and (b)}, three layers {(c) and (d)}, four layers {(e) and (f)}, and six layers {(g) and (h)} (a cutoff of 2 J/m^2 is imposed). For (a), (c), (e), and (g) no relaxation was employed. For (b), (d), (f), and (h), atomic coordinates were relaxed.

relaxed barriers are 0.76 and 0.88 J/m^2 and relaxed barriers are 0.53 and 0.62 J/m^2, respectively. The four-layer barrier is nearly twice as high as these (1.34 J/m^2 unrelaxed and 1.09 J/m^2 relaxed), and two-layer shear was unsuccessful to this point due to atomic overlap. Overall, {111} stacking faults are highly resistant to shear but with relaxation, small fault displacements for three and six layers may facilitate the transformation from B2 to the R phase.

We extrapolate the energy surface and map the Burger's vectors for the relaxed three-layer {111} shear [see Fig. 5(b)], and find that the dislocation process may be split into three primary steps. First, there is a $\langle \bar{2}11 \rangle$ shear to $(\frac{1}{6}a, \frac{1}{6}a)$. The second step proceeds in the $\langle \bar{1}10 \rangle$ direction from $(\frac{1}{6}a, \frac{1}{6}a)$ to $(\frac{5}{6}a, \frac{1}{6}a)$ along a low-energy valley between two unstable superlattice intrinsic stacking faults at $(\frac{1}{3}a, 0)$ and at $(\frac{1}{3}a, \frac{1}{3}a)$. The final partial Burger's vector returns to the original state by means of a $\langle 01\bar{1} \rangle$ shear. Given the large barriers shown here, this transformation clearly cannot occur without other simultaneous mechanisms (e.g., a lattice distortion via Bain strain, a coordinated shearing process involving multiple nonparallel shears, etc.). However, by mapping the dislocation behavior of the system, we expose atomistic transformation properties of the B2 to R martensitic transformation.

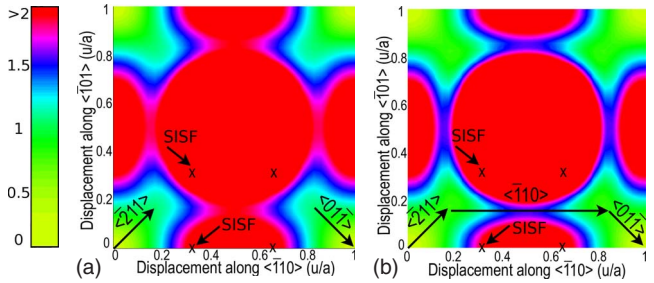

FIG. 5. (Color online) The γ surface for B2 NiTi for (a) full unrelaxed and (b) relaxed three layer {111} slip plane (a cutoff of 2 J/m^2 is imposed).

These calculated γ surfaces can be further used for understanding dislocation and deformation properties of B2 NiTi within atomistic-continuum modeling approaches such as the Peierls-Nabarro (PN) model (see, e.g., Ref. 42). However, even without performing detailed PN modeling, one can predict that due to extremely low shear resistance, ⟨100⟩{011} dislocations will have very low Peierls stress and high mobility while high stress and low mobility occurs in the {001} and {111} fault planes. By mapping the Burger's vectors of the {111} shear plane, quantifying stable and unstable stacking-fault barriers for all major shear planes, and identifying the interplay between shear-layer thickness and barrier height, this data provides both direct guidance into the phase boundary formation and propagation, and indirect inputs for microstructural and continuum modeling that cannot be directly obtained by experiment.

D. Transformation path mechanisms

For many years, researchers have sought a more complete understanding of the atomistic mechanisms in martensite formation primarily for theoretical purposes. Today, the establishment of a more complete theory of martensitic transformation not only has academic importance, it is also instrumental for applied research as it provides theoretical inputs for multiscale modeling approaches to structural behavior. Thus, researchers may model and predict material behavior from the nanoscale to the macroscale. Here we examine the transformation paths of NiTi between its austenitic and martensitic structures.

Since the initial characterization of the phases of martensitic NiTi, researchers have assumed that there is a direct transformation path between the B2 and the B19′ phases that may be inferred from precursor phenomena in the B2 phase. Otsuka and Ren[36] tied the soft C', C_{44}, and TA_2 phonon modes to ⟨1$\bar{1}$0⟩{011} basal shear/shuffle and to ⟨1$\bar{1}$0⟩{001} nonbasal shear instabilities. In turn, these structural instabilities would yield coordinated atomic movements that would transform the B2 to the B19′ phase.

Later, Ye *et al.*[7] modeled a B2 to B19′ transformation by displacing alternating {011} planes while simultaneously imposing an orthorhombic distortion of the unit cell and a distortion of the monoclinic angle to arrive at B19′. However, their *ab initio* pseudopotential calculations showed small energy barriers around the B2 phase. Later, a barrierless path

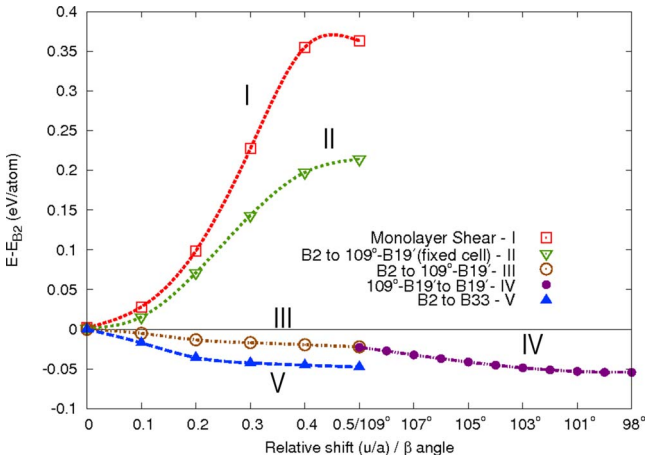

FIG. 6. (Color online) Total energies of the transition mechanisms from B2 to B19′ and the proposed B33 martensitic structures. The B33 and 109°-B19′ structures occur at a relative shear of $\frac{1}{2}\frac{u}{a}$. Lines represent a spline fit to the data points.

from B2 to B33 was found by Morris *et al.*[6] for several B2 intermetallics by shuffling pairs of {011} planes via stacking faults in a B2 supercell. Wang,[43] using the nudged elastic-band method, found a mostly barrierless transformation from B2 to B19′ through a "twinned" structure. However, a small barrier exists between the twinned structure and B19′. Most recently, the present authors found a direct barrierless two-step transformation path from B2 to B19′ through an unstable state, labeled 109°-B19′.[5] Here, we present more details of this path which is composed of a bilayer shear followed by a monoclinic angle relaxation, and we discuss the B2 to B33 transformation path.

The total energies of several transformation paths attempted by us are plotted in Fig. 6. In response to Otsuka and Ren's early suggestion, we performed calculations involving a basal ⟨1$\bar{1}$0⟩{011} shear/shuffle and discovered that there is excessive Ti-Ti repulsion associated with this mechanism. Interatomic repulsion cannot be accommodated by atomic relaxation, prohibiting the calculation of a full transformation path and prompting the conclusion that this transformation cannot be made without impractical energy barriers. We further performed calculations for an alternative path involving a single-layer ⟨100⟩{011} basal shear. Calculations of this path were successful (see path I in Fig. 6) to the unstable stacking fault. However, at this point we found significantly high-energy barriers of around 37 meV/atom above the B2 phase due to Ti-Ni repulsive forces. Thus, these findings show that monolayer shears applied to the B2 phase are improbable as an initial component of the transformation path.

Considering that low unstable stacking-fault energy barriers were obtained in our {011} γ-surface calculations, we explore mechanisms which use this shear. The lowest barriers were obtained using ⟨100⟩{011} shear, and of the thinner slabs, two layers had the lowest-energy barriers (see Table VI). Thus, we calculate a bilayer ⟨100⟩{011} basal shear/shuffle from the B2 phase to a shuffle of $0.5\frac{u}{a}$ (see path II in Fig. 6). While all the atomic coordinates were relaxed throughout this process, we fixed the dimensions of the unit

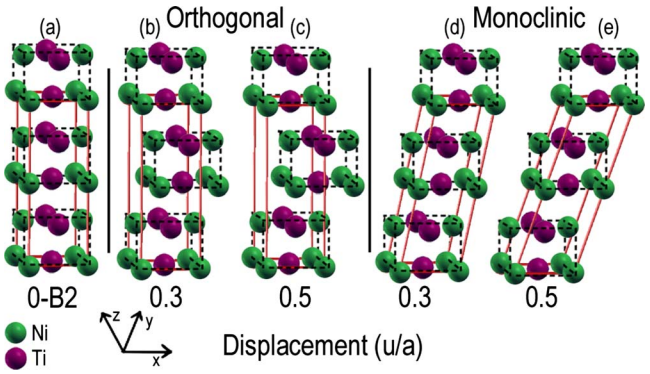

FIG. 7. (Color online) The NiTi B2 phase viewed along the {011} plane for the bilayer transformation path to $\frac{1}{2}a\{011\}$ shear. No relaxation is employed. The initial structure of B2 NiTi is shown as 0 displacement, and imposed shears of 0.3 and 0.5 times the lattice constant are shown next for an orthorhombic and monoclinic unit cell. The structures are equivalent at the 0.5 point. Solid lines outline the unit cell and dotted lines outline the bilayers.

cells and an energy barrier of 0.22 eV/atom was found. However, when *all* lattice constants and full atomic coordinate relaxation were employed, the transformation path become barrierless to $0.5\frac{u}{a}$ (see path III in Fig. 6).

For this path, two different shearing mechanisms were used and are compared here. These mechanisms are illustrated in Fig. 7 (without relaxation) such that the {011} plane is perpendicular to the vertical axis at each displacement step and the stacking fault between each pair of planes is induced in the ⟨100⟩ direction. For the first mechanism, the initial B2 phase, $Pm\bar{3}m$ space group, is distorted by applying a bilayer ⟨100⟩{011} basal shear/shuffle to a four-atom supercell. This breaks its cubic symmetry and the system becomes orthorhombic (space group *Pcam*). By allowing atomic relaxation [see Figs. 8(a)–8(c)], when the shuffle reaches $0.5\frac{u}{a}$ displacement, the primitive unit cell becomes equivalent to the monoclinic type B19′ (space group $P2/1m$). This metastable phase is equivalent to the martensite phase, except for the monoclinic angle, β, which is 109°, and we name this phase 109°-B19′. The second mechanism is also modeled with a four-atom supercell but instead of shuffling the atoms in a fixed orthorhombic supercell, we apply a monoclinic shear to

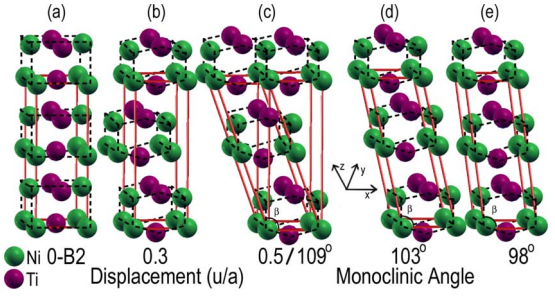

FIG. 8. (Color online) The transformation path from B2 to B19′. The path proceeds with a bilayer shear of 0.3 and 0.5 times the lattice constant. At $\frac{1}{2}a\{011\}$ shear, the structure is monoclinic with an angle β of 109°. The monoclinic angle is relaxed and brings this structure to B19′ at 98°.

the unit cell. By doing this, the long-range order is monoclinic, although at $0.5u/a$ displacement, the exact same crystal structure is obtained, including the long-range order of the system. Thus, in the first method bilayers are sheared in opposite directions while in the second method bilayers are sheared in the same direction. Despite the differences in long-range order throughout the transformation, these shearing mechanisms yielded identical results within numerical error. Thus, the transformation path is continuous and barrierless to 109°-B19′ and the final total energy is 25.2 meV/atom lower than B2 (see path III in Fig. 6).

At this point, we note that B19′ has a lower total energy than this devised intermediate phase, 109°-B19′. Thus, the transformation must proceed to the more stable structure. It is easily determined that the primary difference between these two structures was their respective monoclinic angles, β. For path IV [see Fig. 6 and Fig. 8(c)–8(e)] we relax the β angle of 109°-B19′ to β=98°, which effectively induces a ⟨100⟩{011} basal shear and the structure becomes B19′. As shown in Fig. 6, this angle relaxation is barrierless and completes the transformation to B19′. By combining paths III and IV, we have established a direct continuous barrierless transformation path from the B2 phase to the B19′. The transformation between these phases consists of a ⟨100⟩{011} bilayer basal shear/shuffle followed by another basal shear which relaxes the structure's monoclinic angle. The resultant phase is the experimentally observed B19′ phase which has a total energy that is 55.4 meV/atom below B2.

This barrierless path was calculated with the omission of temperature effects. If temperature effects were included, the B2 phase would become stabilized entropically, and at temperatures above the martensitic transformation temperature, the free energy of the martensite would be higher than that of the austentite. Our calculations simulate the cooling process whereby the entropic stabilization of the austenite reduces and vanishes, revealing the barrierless transformation path that we have described. Since total-energy DFT calculations by definition describe ground-state (T=0 K) properties of materials, these calculations cannot address the free-energy stabilization of the B2 phase directly. However, several combined techniques which integrate DFT calculations with atomic dynamics to investigate thermal excitations, e.g., high-temperature phonon calculations based on self-consistent *ab initio* lattice dynamics[44] or *ab initio* molecular-dynamics simulations,[45,46] may obtain temperature-dependent free energies which quantify this effect. The application of temperature effects, however, lies beyond the scope of the present study, in which we focus on intrinsic structural and mechanical properties of the NiTi phases that enable the transformation path as the austenite transforms to martensite.

The primary reordering during relaxation is exemplified by comparing Ni-Ti interatomic distances. Without relaxation, the interatomic distance for Ni-Ti across the slip plane and within the bilayers is 2.13 and 2.61 Å, respectively, at $\frac{u}{a}\langle 100\rangle\{011\}$ shear [see Fig. 7(c)]. After optimization at this point, the distances change to 2.44 Å across the plane and 2.50 and 2.60 Å within the bilayer [see Fig. 8(c)]. As the angle β in NiTi becomes 98°, and NiTi becomes B19′, the Ni-Ti distance equivalent to those across the slip plane for

B19′-109° (which was formerly 2.44 Å) becomes 2.59 Å, and the two Ni-Ti distances (formerly 2.50 and 2.60 Å) that were within the bilayer become 2.53 and 2.60 Å (see Fig. 8). Thus, through this process, the bond distances equalize after departing from the highly symmetric B2 cubic structure at which Ni-Ti distances were 2.61 Å. The final Ni-Ti distances for B19′ are 2.53, 2.59, and 2.60 Å.

As noted above and in Sec. I, Huang *et al.*[2] asserted that the true low-energy structure was B33, and that the angle β of B19′ was susceptible to elongation and was stabilized by internal stresses. This has been subsequently verified by other calculations.[4,6,47] Our calculations agree: by optimizing all lattice constants and atomic coordinates, the monoclinic angle of B19′ may be increased to form B33. Using the structural parameters provided by Huang *et al.*, we determined that the total energy of the B33 phase is 4.6 meV/atom lower than the B19′ phase. While lower, this energy difference is very small (~50 K), and further study concerning its relation to the B2 structure is warranted. Additionally, while the primitive unit cell is similar to the B19′ structure, it has a larger monoclinic angle and the volume of the B33 unit cell is greater than that of B19′ due to a large elongation of the a lattice constant.

Since the B33 phase has been established as the low-energy phase, why is it not found in experimental measurements? To answer this question, we calculated a transformation path from the B2 to the B33 phase (see path V in Fig. 6). The B33 phase was reached at bilayer $\frac{1}{2}\frac{u}{a}\langle 100\rangle\{011\}$ shear but relaxation caused an impractical 10.1% elongation of the a lattice constant when the final structure was reached. This expansion of a occurred immediately whereas for path III, $0.1\frac{u}{a}$ shear had caused an a lattice expansion of 1%; for path V, a was nearly 4% longer. Given this elongation, it is improbable that such a transformation would occur within a bulk system. Instead, the system is likely to stabilize the B19′ phase with internal stresses (as has been proposed[2] and quantified[4]), and the B2→B19′ transformation will follow our calculated path (III+IV) in which no lattice constant is distorted by more than 3%.

Thus, B33 may form in certain environments with minimized internal stresses. It prefers a greater lattice elongation throughout the martensitic transformation. While we have predicted that the direct path from B2 to the B33 phase is energetically favorable, the direct transformation path from the B2 phase to the B19′ phase is still preferred in the bulk system because it does not require large lattice distortions.

IV. SUMMARY AND CONCLUSION

We have calculated the structure of equiatomic NiTi for each of the experimentally and theoretically suggested crystal structures. Using structural optimization, we find total energies and lattice constants to be in agreement with previous calculations and experimental findings. We confirm the existence of the B33 phase and obtain similar results in comparison with previous calculations. The formation energy has been calculated and is in closer agreement with experiment than previous calculations and we present formation energies for intermediate and martensitic structures.

For the R phase of NiTi, our total-energy results indicate that the most favorable space group is $P3$, first experimentally observed by Hara *et al.*; Schryvers *et al.*, measured a $P\bar{3}$ space group for the R phase alloyed with iron. We found that space group $P\bar{3}$ is a metastable state. However, the structure with this symmetry was less stable than the $P3$ space-group structure as its total energy was higher by 3 meV/atom. Since alloying can change the structure of a material, these results are not necessarily contradictory; instead, small amounts of iron may change the symmetry of the R phase to $P\bar{3}$.

We compared all the elastic constants calculated for the B2, R, B19, B19′, and B33 structures. We asserted that restricting geometry optimization gives insights into entropically stabilized metastable states—as is shown for the B2, B19, and B19′ phases via the stability of the C' and C_{55} elastic constants. The C' value, which must be positive for stable structures, is 19 GPa for the B2 phase, which agrees with experiment within 11%. For B19, B19′, and B33 stability against monoclinic deformation is linked to the C_{55} elastic constant, which is positive for each of these structures. Additionally, the calculated elastic constants of R are reported. The B2 phase has lower C_{44} and C' values than other phases, suggesting that these soft elastic constants are a precursor to the martensitic transformation. Supporting experimental findings of Brill *et al.*, we find a sharp decrease in the anisotropy factor from the B2 structure to other structures.

Macroscopic elastic moduli which describe polycrystalline samples may also be obtained through an analysis of the single-crystal elastic constants, and the bulk, shear, and Young's moduli and Poisson's ratio have been calculated and presented. Our calculated Young's modulus of the B2 and B19′ phases agrees well with experiment, and we have analyzed these elastic properties to learn about the macroscopic behavior of NiTi. Unlike the B2 phase, the B19′ phase exhibits a higher stiffness and a high shear modulus, which stabilizes it with respect to other phases including B33. Additionally, we have identified indicators which suggested that B19′ is ductile and less susceptible to crack formation. Due to the good stability and high ductility of this martensitic phase, desirable mechanical properties for shape-memory alloys are achieved in the NiTi system. Additionally, these theoretical single-crystal and polycrystalline elastic constants provide inputs for larger scale modelling approaches and as such may be used to predict macroscopic behavior.

Generalized stacking-fault (γ-surface) calculations were performed for the {001}, {011}, and {111} slip planes of B2. We clearly illustrated stacking-fault instabilities, energy barriers, and their relation to stacking-fault layer thicknesses. We found a sharp resistance to {001} and {111} shear which is lowered by relaxation but remains strong; {001} faults are unlikely to occur. For the {111} slip plane, slip likely occurs with three- or six-atom layer thicknesses in the $\langle\bar{2}11\rangle$ direction but shears of more than $0.2\frac{u}{a}$ are unlikely. Nevertheless, the Burger's vectors for this system have been mapped with the expectation that coordinated shear/strain behavior may allow dislocations and transform B2 to R.

Resistance to {011} shear is significantly lower. After fully relaxing the atomic coordinates in the perpendicular direc-

tion, we found very low-energy barriers to stacking faults in the ⟨100⟩ direction of this plane. Stable stacking faults occurred at $\frac{1}{2}\frac{u}{a}\langle 100\rangle\{011\}$, and this barrier height was lowest for the two-, four-, and six-layer cases. Thus, for these thicknesses, an instability was likely if lattice constants or additional parameters were relaxed, and these results prompted a search for transformation paths using similar mechanisms.

Finally, after reviewing and attempting previously proposed transformation paths, we establish the direct mechanisms of martensitic transformation. We predicted a two-step transformation for NiTi between the B2 austenitic and B19′ martensitic phases and a one-step transformation between the B2 and B33 phases. The B2 to B33 transformation is accomplished by a bilayer in the ⟨100⟩{011} direction and is facilitated by an elongation of the a lattice constant, which is not likely to be allowed in a bulk system. The B2 to B19′ transformation occurs through bilayer ⟨100⟩{011} shear followed by a relaxation of the angle β. Throughout the bilayer shearing process, there is a sizeable rearrangement of the atomic positions in the c direction, which allows the transformation to occur without overlap between atoms and minimizes changes to the interatomic distances. The relaxation of β continues to equalize these distances and the transformation is completed when this angle reaches 98°. The final martensitic phase is the B19′ structure which is 55 meV/atom lower in energy than the B2 phase.

ACKNOWLEDGMENTS

This work was supported by the AFOSR (Grant No. FA9550-07-1-0174), the ONR (Grant No. N00014-05-C-0241), and the NASA Graduate Student Researchers Program. Computer time was provided by DOD HPC centers NAVO, ARSC, ASC, and MHPCC under Grants No. AFOSR15573FR1 and No. ONRDC07319050.

APPENDIX: DETAILS OF ELASTIC CONSTANT CALCULATIONS

The single-crystal elastic constants presented here were calculated using the formalism proposed by Wallace.[48] These are calculated by first creating a symmetric distortion matrix $\hat{e}$,

$$\hat{e} = \begin{pmatrix} 1+a_{xx} & a_{xy} & a_{xz} \\ a_{yx} & 1+a_{yy} & a_{yz} \\ a_{zx} & a_{zy} & 1+a_{zz} \end{pmatrix}, \tag{2}$$

where $a_{ij}=a_{ji}$. Exploiting this symmetry, we may replace a_{ij} with α_k, where $k=1$ to 6. Thus, $a_{xx}=\alpha_1$, $a_{yy}=\alpha_2$, $a_{zz}=\alpha_3$, $a_{xy}=a_{yx}=\alpha_4$, $a_{yz}=a_{zy}=\alpha_5$, and $a_{zx}=a_{xz}=\alpha_6$. A distortion matrix, with certain α_i values chosen as nonzero, is multiplied by the Bravais lattice matrix,

$$\hat{L} = \begin{pmatrix} L_{1x} & L_{1y} & L_{1z} \\ L_{2x} & L_{2y} & L_{2z} \\ L_{3x} & L_{3y} & L_{3z} \end{pmatrix}, \tag{3}$$

to obtain a distorted unit cell. To calculate the elastic constants, we expand the total energy in a Taylor series with respect to this distorted unit cell. The total energy to second order is

$$E(V,\alpha) = E(V_o,0) + V_o\left(\sum_i \tau_i\alpha_i + \frac{1}{2}\sum_{i,j} C_{ij}\alpha_i\xi_i\alpha_j\xi_j\right). \tag{4}$$

The expansion coefficients, τ and C_{ij}, are the stress-tensor components and elastic constants. If a stable structure has been obtained, the stress-tensor components will be negligible, as we found in our calculations. As for α, the indices of the elastic constants, i and j, run from 1 to 6. There are up to 21 independent elastic constants given in Voigt notation which have been tabulated by Wallace[48] for each crystal symmetry. The variable ξ is used to take into account constants which need to be double counted for $i=4,5,6$; $\xi=2$, and for $i=1,2,3$; $\xi=1$. The elastic constants are determined by finding $\frac{d^2E(V,\alpha)}{d\alpha^2}$. This is accomplished by creating a distortion matrix for each independent elastic constant. In our calculations, α ranged from −2.5% to 2.5% in steps of 0.5%.

As an example, for the orthorhombic B19 structure, space group $Pcmm$, there are nine independent elastic constants: C_{11}, C_{12}, C_{13}, C_{22}, C_{23}, C_{33}, C_{44}, C_{55}, and C_{66}. To calculate C_{66} we compose the distortion matrix,

$$\hat{e} = \begin{pmatrix} 1 & 0 & 0 \\ 0 & 1 & \alpha \\ 0 & \alpha & 1 \end{pmatrix}. \tag{5}$$

For this distortion matrix, the total energy is

$$E(V,\alpha) = E(V_o,0) + V_o(\tau_6\alpha + 2C_{66}\alpha^2). \tag{6}$$

The total energies are fit to this equation with a second-order polynomial fit. However, for each elastic constant, there are several different combinations of distortions that may be used to obtain data points and an equation of fit. To calculate C_{12}, we choose the distortion matrix,

$$\hat{e} = \begin{pmatrix} 1+\alpha & 0 & 0 \\ 0 & 1+\alpha & 0 \\ 0 & 0 & 1 \end{pmatrix}. \tag{7}$$

The total energy becomes

$$E(V,\alpha) = E(V_o,0) + V_o\left[(\tau_1+\tau_2)\alpha + \frac{1}{2}(C_{11}+2C_{12}+C_{22})\alpha^2\right]. \tag{8}$$

Since C_{12} is dependent on C_{11} and C_{22}, we must create two additional distortion matrices to calculate those constants in order to solve C_{12}. A total of nine independent distortion matrices are needed to obtain each of the independent elastic constants for the orthorhombic structure. This procedure was carried out for each structure. There are three independent elastic constants for the B2 cubic structure, 13 for monoclinic B19′, and six for each R structure given its hexagonal symmetry. These values are shown in Table IV. Additionally, for each of these structures, we have tabulated C', the Zener anisotropy (A), and the bulk moduli (B), which were calculated by fitting volume distortions to the Birch-Murnaghan equation of state.[25]

C' is typically defined for cubic structures as $C' = \frac{(C_{11}-C_{12})}{2}$ but this stability may be generalized to orthorhombic structures[4] as the minimum value of several possible distortions, namely,

$$4C' = \begin{cases} C_{11}+C_{22}-2C_{12} \\ C_{11}+C_{33}-2C_{13} \\ C_{22}+C_{33}-2C_{23} \\ C_{11}+C_{22}+C_{33}+2C_{12}+2C_{13}+2C_{23} \end{cases}, \quad (9)$$

where instability occurs for $C'<0$. We note that the efficacy of C' for monoclinic structures has not been established but we include them for comparison.

A is defined for cubic structures as C_{44}/C'. However, in more complex phases, this may be generalized to the minimum value of three separate equations,

$$A = \begin{cases} C_{44}/C' \\ C_{55}/C' \\ C_{66}/C' \end{cases}. \quad (10)$$

For the polycrystalline elastic moduli, we refer to Hill,[49] who examined two competing elastic-constant calculation techniques, that of Voigt,[50] who built a formalism based on an assumption of uniform strain throughout a sample, and of Reuss,[51] who assumed uniform stress. Hill proved that these two values constituted bounds of the actual elastic moduli, which could be accurately estimated as the midpoint between these two values (the Hill averages).

The Voigt and Reuss bulk and shear moduli are

$$9B_V = (C_{11}+C_{22}+C_{33}) + 2(C_{12}+C_{23}+C_{31}), \quad (11)$$

$$15G_V = (C_{11}+C_{22}+C_{33}) - (C_{12}+C_{23}+C_{31}) + 3(C_{44}+C_{55}+C_{66}), \quad (12)$$

$$\frac{1}{B_R} = (S_{11}+S_{22}+S_{33}) + 2(S_{12}+S_{23}+S_{31}), \quad (13)$$

$$\frac{15}{G_R} = 4(S_{11}+S_{22}+S_{33}) - 4(S_{12}+S_{23}+S_{31}) + 3(S_{44}+S_{55}+S_{66}), \quad (14)$$

where C_{ij} are the single-crystal elastic constants, S_{ij} are components of the compliance matrix, $c^{-1}=s$, the inverse of the elastic constant matrix, and K and G are the bulk and shear moduli using the Voigt and Reuss formalism. The Hill average is therefore, $B=\frac{1}{2}(B_V+B_R)$ and $G=\frac{1}{2}(G_V+G_R)$.

Poisson's ratio (ν) and Young's modulus are calculated as follows:

$$\nu = \frac{1}{2}\left[1 - \frac{3G}{3B+G}\right], \quad (15)$$

$$\frac{1}{E} = \frac{1}{3G} + \frac{1}{9B}. \quad (16)$$

Young's modulus may be calculated by using Hill averaged values, Reuss moduli, or Voigt moduli. All three have been presented. The Poisson's ratio was calculated using Hill averaged values for the shear and bulk moduli.

[1] R. Vogel and H. J. Wallbaum, Arch. Eisenhuettenwes. **12**, 299 (1938).
[2] X. Huang, G. Ackland, and K. Rabe, Nature Mater. **2**, 307 (2003).
[3] C. Gong, Y. Li, Y. Yang, and D. Yang, Modell. Simul. Mater. Sci. Eng. **14**, 33 (2006).
[4] M.-X. Wagner and W. Windl, Acta Mater. **56**, 6232 (2008).
[5] N. Hatcher, O. Y. Kontsevoi, and A. J. Freeman, Phys. Rev. B **79**, 020202(R) (2009).
[6] J. R. Morris, Y. Y. Ye, M. Krcmar, and C. L. Fu, in *Advanced Intermetallic-Based Alloys*, edited by J. Wiezorek, C. L. Fu, M. Takeyama, D. Morris, and H. Clemens, MRS Symposia Proceedings, Vol. 980 (Materials Research Society, Warrendale, PA, 2007), p. II06–10.
[7] Y. Y. Ye, C. T. Chan, and K. M. Ho, Phys. Rev. B **56**, 3678 (1997).
[8] F. E. Wang, S. J. Pickart, and H. A. Alperin, J. Appl. Phys. **43**, 97 (1972).
[9] G. M. Michal and R. Sinclair, Acta Crystallogr., Sect. B: Struct. Crystallogr. Cryst. Chem. **37**, 1803 (1981).
[10] P. Sittner, P. Lukás, D. Neov, V. Novák, and D. M. Toebbens, J. Phys. IV **112**, 709 (2003).
[11] T. Hara, T. Ohba, E. Okunishi, and K. Otsuka, Mater. Trans., JIM **38**, 11 (1997) .
[12] D. Schryvers and P. Potapov, Mater. Trans., JIM **43**, 774 (2002).
[13] T. Nam, T. Saburi, Y. Nakata, and S. Shimizu, Mater. Trans., JIM **31**, 1050 (1990).
[14] T. Ohba, T. Taniwaki, H. Miyamoto, K. Otsuka, and K. Kato, Mater. Sci. Eng., A **438-440**, 480 (2006).
[15] R. Zarnetta, E. Zelaya, G. Eggeler, and A. Ludwig, Scr. Mater. **60**, 352 (2009).
[16] M. Panduranga, D. Shin, and G. Carman, Thin Solid Films **515**, 1938 (2006).
[17] S. Prokoshkin, A. Korotitskiy, V. Brailovski, S. Turenne, I. Khmelevskaya, and I. Trubitsyna, Acta Mater. **52**, 4479 (2004).
[18] Y. Kudoh, M. Tokonami, S. Miyazaki, and K. Otsuka, Acta Metall. **33**, 2049 (1985).
[19] M. Sanati, R. C. Albers, and F. J. Pinski, Phys. Rev. B **58**, 13590 (1998).
[20] K. Parlinski and M. Parlinska-Wojtan, Phys. Rev. B **66**, 064307 (2002).
[21] S. Ishida and S. Asano, Mater. Trans. **43**, 780 (2002).
[22] E. Wimmer, H. Krakauer, M. Weinert, and A. J. Freeman, Phys. Rev. B **24**, 864 (1981).
[23] J. P. Perdew, K. Burke, and M. Ernzerhof, Phys. Rev. Lett. **77**, 3865 (1996).
[24] M. Weinert, G. Schneider, R. Podloucky, and J. Redinger, J. Phys.: Condens. Matter **21**, 084201 (2009).

[25] F. Birch, Phys. Rev. **71**, 809 (1947).
[26] E. Goo and R. Sinclair, Acta Mater. **33**, 1717 (1985).
[27] T. Kawamura, R. Tachi, T. Inamura, H. Hosoda, K. Wakashima, K. Hamada, and S. Miyazaki, Mater. Sci. Eng., A **438-440**, 383 (2006).
[28] R. F. Hehemann and G. D. Sandrock, Scr. Mater. **5**, 801 (1971).
[29] X. Huang, H.-J. Lee, and A. G. Ramirez, Scr. Mater. **59**, 1067 (2008).
[30] J. Gachon, M. Notin, and J. Hertz, Thermochim. Acta **48**, 155 (1981).
[31] O. Kubaschewski, Trans. Faraday Soc. **54**, 814 (1958).
[32] A. Pasturel, C. Colinet, D. N. Manh, A. T. Paxton, and M. van Schilfgaarde, Phys. Rev. B **52**, 15176 (1995).
[33] T. M. Brill, S. Mittelbach, W. Assmus, M. Müllner, and B. Lüthi, J. Phys.: Condens. Matter **3**, 9621 (1991).
[34] O. Mercier, K. N. Melton, G. Gremaud, and J. Häji, J. Appl. Phys. **51**, 1833 (1980).
[35] Q. M. Hu, R. Yang, J. M. Lu, L. Wang, B. Johansson, and L. Vitos, Phys. Rev. B **76**, 224201 (2007).
[36] K. Otsuka and X. Ren, Mater. Sci. Eng., A **273-275**, 89 (1999).
[37] C. Fu, J. Mater. Res. **5**, 971 (1990).
[38] K. Gschneidner, A. Russell, A. Pecharsky, J. Morris, Z. H. Zhang, T. Lograsso, D. Hsu, H. C. Lo, Y. Y. Ye, A. Slager, and D. Kesse, Nature Mater. **2**, 587 (2003).
[39] M. Achenbach, Int. J. Plast. **5**, 371 (1989).
[40] S. Rajagopalan, A. Little, M. Bourke, and R. Vaidyanathan, Appl. Phys. Lett. **86**, 081901 (2005).
[41] V. Vitek, Cryst. Lattice Defects **5**, 1 (1974).
[42] N. I. Medvedeva, O. N. Mryasov, Y. N. Gornostyrev, D. L. Novikov, and A. J. Freeman, Phys. Rev. B **54**, 13506 (1996).
[43] X.-Q. Wang, Phys. Rev. B **78**, 092103 (2008).
[44] P. Souvatzis, O. Eriksson, M. I. Katsnelson, and S. P. Rudin, Phys. Rev. Lett. **100**, 095901 (2008).
[45] V. Ozolins, Phys. Rev. Lett. **102**, 065702 (2009).
[46] C. Asker, A. B. Belonoshko, A. S. Mikhaylushkin, and I. A. Abrikosov, Phys. Rev. B **77**, 220102(R) (2008).
[47] G. J. Ackland, A. P. Jones, and R. Noble-Eddy, Mater. Sci. Eng., A **481-482**, 11 (2008).
[48] D. Wallace, *Thermodynamics of Crystals* (Wiley, New York, USA, 1972).
[49] R. Hill, Proc. Phys. Soc., London, Sect. A **65**, 349 (1952).
[50] W. Voigt, *Lehrbuch der kristallphysik* (Leipzig, Berlin, 1910).
[51] A. Reuss, Z. Angew. Math. Mech. **9**, 49 (1929).